Nanoscale

PAPER

View Article Online
View Journal | View Issue

Cite this: *Nanoscale*, 2018, **10**, 741

In situ carbon encapsulation of vertical MoS_2 arrays with SnO_2 for durable high rate lithium storage: dominant pseudocapacitive behavior†

Mengjiao Li,[a,b] Qinglin Deng,[a,b] Junyong Wang,[a,b] Kai Jiang,[a,b] Zhigao Hu *[a,b] and Junhao Chu[a,b]

Improving the conductivity and charge transfer kinetics is favourable for innovation of sustainable energy devices such as metal oxide/sulfide-based electrodes. Herein, with an intercalation pseudocapacitance effect, an *in situ* polymerization–carbonization process for novel carbon-sealed vertical MoS_2–SnO_2 anchored on graphene aerogel (C@MoS_2–SnO_2@Gr) has enabled excellent rate performance and durability of the anode of lithium ion batteries to be achieved. The integrated carbon layer and graphene matrix provide a bicontinuous conductive network for efficient electron/ion diffusion pathways. The charge transfer kinetics could be enhanced by the synergistic effects between vertical MoS_2 nanosheets and well-dispersed SnO_2 particles. Based on the crystal surface matching, the ameliorated electric contact between MoS_2 and SnO_2 can promote the extraction of Li^+ from Li_2O and restrain the serious aggregation of Li_xSn. As a result, the improved reversibility leads to a higher initial coulombic efficiency (ICE) of 80% (0.1 A g^{-1} current density) compared to that of other materials. In particular, with the dominating surface capacitive process, the C@MoS_2–SnO_2@Gr electrode delivers a stable capacity of 680 mA h g^{-1} at 2.5 A g^{-1} for 2000 cycles. Quantitative insight into the origin of the boosted kinetics demonstrated the high pseudocapacitance contribution (above 90%) which leads to the durable high rate Li ion storage.

Received 3rd October 2017,
Accepted 27th November 2017

DOI: 10.1039/c7nr07359c

rsc.li/nanoscale

1. Introduction

Due to energy consumption and widespread portable electronic equipment, lithium ion batteries (LIBs), as one of the most practical energy storage systems, have been intensely studied due to their high capacity and rate capability.[1–5] Taking the lower power density of conventional graphite into consideration, a variety of semiconductor materials including carbon-based and metal/alloy-based anodes could be ideal candidates.[6–9] In particular, abundant transition metal oxides/sulfides, applicable to both the conversion and alloying reaction, show obvious advantages in Li ion storage. MoS_2 is known to have large interlamellar spacing, better carrier mobility, and a higher exposed surface area, which are favourable for fast Li^+ insertion/desertion and reversibility.[10–13] However, the special stacked layers with van der Waals interactions make MoS_2 have a tendency to self-aggregate to minimize the surface energy during the synthetic or storage process. Also, the electron/ion transfer kinetics would be limited by its poor conductivity, which affects the durability for long-term cycling.[14–16] In particular, recent work by Chen *et al.* on novel oxide electrodes for applications in LIBs with excellent high-rate and long-life performance further verified the vital role of boosted conductivity and charge transfer kinetics.[17–21] Therefore, the lack of a unique structure and beneficial mechanism becomes the intrinsic drawback to the use of MoS_2-based electrodes.

Generally, graphene and carbon cloths with numerous active sites can act as an available conductive skeleton and buffer to mechanical stress for cycling stability. To the best of our knowledge, several improved MoS_2/graphene electrodes have been reported, such as ones with a high reversible capacity of 1200 mA h g^{-1} or 60% capacity retention after hundreds of cycles.[22,23] However, at high-rate evaluation, MoS_2 sheets usually re-stack into big clusters on graphene due to the similar interactions, which means that serious aggregation cannot be avoided. Fortunately, it has been demonstrated that vertically aligned nano-arrays on graphene can effectively

[a]*Key Laboratory of Polar Materials and Devices (MOE) and Technical Center for Multifunctional Magneto-Optical Spectroscopy, Shanghai, China*
[b]*Department of Electronic Engineering, East China Normal University, Shanghai 200241, China. E-mail: zghu@ee.ecnu.edu.cn; Fax: +86-21-54345119; Tel: +86-21-54345150*

†Electronic supplementary information (ESI) available. See DOI: 10.1039/c7nr07359c

enlarge the interfacial contact and structural separation in the volume to improve charge transfer and reaction kinetics.[24–29] In addition, with two-times the lithium storage ability of graphite, typical alloy-based anode SnO_2 can be facilely prepared through a simple hydrolysis process of $SnCl_4{\cdot}5H_2O$, from which the colloidal SnO_2 precursor provides beneficial viscous force for the vertical growth of MoS_2 nanosheets.[30–33] According to the band structure, SnO_2 can also form a unique p–n junction with MoS_2 for built-in electric force. Thus, it is believed that SnO_2 is a suitable partner for MoS_2 to construct a novel architecture for considerable synergistic kinetics.[34–36] At present, the energy storage mechanisms can be classified as a diffusion-controlled process and surface capacitive process.[37–39] For the former, a high rate capacity cannot be obtained because of the worse mass transportability into the bulk, while the latter involves both the double layer capacitance (non-faradaic) and the faradaic contribution, which is beneficial for fast capacitive reactions and enhanced rate capability. Therefore, for alloy-based SnO_2 anodes, the pseudocapacitance contribution can be distinctly created from ultrafine particles and an ultralarge reaction surface.[40,41] In terms of the above, more attention should be concentrated on building a novel structure and reliable capacitive kinetics for improved anodes.

With the aim of improving the conductivity and enhancing the reaction kinetics, an integrated architecture of carbon-sealed vertical MoS_2–SnO_2 distributed on 3D graphene aerogel was proposed, synthesized through simple vapor polymerization/carbonization procedures. The novel heterostructure with intimate contact between vertical MoS_2 sheets and fine SnO_2 particles could effectively enhance the charge transfer kinetics for Li ion storage. In particular, the built-in electric field force can facilitate electron/ion diffusion and avoid the localized formation of Li_2O. As a result, a higher ICE (80%) was obtained due to the ameliorated reversible conversion, which showed a 20% improvement over MoS_2@Gr. Significantly, a surface capacitive-dominated reaction is favourable for fast kinetics and excellent rate performance, and 680 mA h g^{-1} remained after 2000 cycles at 2.5 A g^{-1}. The boosted lifetime at high GDC derived from the 90% pseudocapacitance contribution indeed provides the opportunity for using transition metal-based anodes in practical Li^+ storage applications.

2. Experimental details

Preparation of MoS_2–SnO_2@Gr

Graphene oxide (GO) was synthesized by a modified Hummers' method with graphite nanoflakes. MoS_2–SnO_2@Gr was prepared by a facile hydrothermal method.[42] Typically, 0.18 g $SnCl_4{\cdot}5H_2O$, 0.24 g $Na_2MoO_4{\cdot}2H_2O$, and 0.14 g thiourea were dissolved in 10 mL deionized water (DI) and stirred uniformly as solutions A, B, and C, respectively. Then the above solutions were successively added into 10 mL homogeneous GO solution (2 mg mL^{-1}) under strong magnetic stirring for 2 h. Finally, the mixed chocolate-coloured solvent was transferred into a 50 mL Teflon-lined stainless steel autoclave and hydrothermally treated at 180 °C for 18 h. After being cooled down to room temperature, the jelly-like cylinder-shaped resultant product was collected and washed with DI water several times, then freeze-dried for 30 h. To obtain MoS_2–SnO_2@Gr, an annealing treatment was performed under argon for 3 h.

Preparation of C@MoS_2–SnO_2@Gr

In brief, the as-synthesized MoS_2–SnO_2@Gr was put into the top of a sealed 500 mL beaker pre-filled with pyrrole. After a vapor phase polymerization process at 70 °C, the resultant product was obtained as ppy-MoS_2–SnO_2@Gr. Next, the above sample underwent carbonization treatment at 450 °C for 3 h with argon as the protective gas to get the final carbon layer-encapsulated MoS_2–SnO_2@Gr heterostructure (C@MoS_2–SnO_2@Gr).

Preparation of MoS_2–SnO_2, MoS_2Gr, and SnO_2@Gr

Generally, the MoS_2–SnO_2 hybrid could be obtained with the same method as that used for MoS_2–SnO_2@Gr, apart from adding GO solution. MoS_2Gr was synthesized from GO, $Na_2MoO_4{\cdot}2H_2O$, and thiourea. SnO_2@Gr was also obtained in a similar way with GO and $SnCl_4{\cdot}5H_2O$.

Sample characterization

The crystallinity and purity of the resulting products were characterized using X-ray diffraction (XRD, Bruker D8 Advance diffractometer) with Cu Kα radiation (λ = 1.5418 Å). Field emission scanning electron microscopy (FESEM, JEOL-JSM-6700F) was employed to investigate the morphological features of the samples, equipped with energy dispersive X-ray spectroscopy (EDS). The high resolution transmission electron microscopy (HRTEM) and elemental mapping studies were carried out at an accelerating voltage of 200 kV to gain detailed insight into the crystal structure of C@MoS_2–SnO_2@Gr. Raman spectroscopy experiments were conducted using a Jobin–Yvon LabRAM HR 800 micro-Raman spectrometer. X-ray photoelectron spectroscopy (XPS, RBD upgraded PHI-5000C ESCA system, PerkinElmer) analysis was carried out with Mg Kα radiation ($h\nu$ = 1253.6 eV). The specific surface area was calculated using the Brunauer–Emmett–Teller (BET) method (TriStar II 3020, America). Thermogravimetric analysis (TGA, TA Instruments 2000) was performed from 60–800 °C in air, at a heating rate of 10 °C min^{-1}.

Electrochemical measurements

For the LIB system test, the working electrode was prepared by dispersing the as-fabricated samples, acetylene black, and poly (vinyl-difluoride) (PVDF) with a weight ratio of 8 : 1 : 1 in *N*-methy-2-pyrrolidone (NMP) under magnetic stirring. Then the slurry was uniformly pasted onto Cu foil and dried in a vacuum oven at 90 °C overnight. The mass of each electrode with a diameter of 12 mm was about 0.8 mg cm^{-2}. Note that the mass with about 2.5 mg cm^{-2} also be prepared for controlled experiments. For electrochemical measurements, the CR2025-type coin cells were assembled in an argon-filled glove

box (Mikrona, Germany) with Li foil as the counter electrode. The Celgard 2400 membrane and 1 M $LiPF_6$ in ethylene carbonate/dimethyl carbonate/ethyl methyl carbonate (1 : 1 : 1 in volume) were used as the separator and electrolyte, respectively. Galvanostatic cycling tests of the as-assembled batteries were conducted in the voltage range of 0.02–3.0 V (*vs.* Li^+/Li) using the Land Battery-Testing station. Cyclic voltammetry (CV) (a scan rate of 0.5 mV^{-1}) and electrochemical impedance spectroscopy (EIS) (a frequency range of 0.01–100k Hz) were recorded on a CHI660E electrochemical workstation.

3. Results and discussion

The fabrication procedure of the integrated carbon-coated MoS_2–SnO_2 based on the 3D graphene aerogel architecture is illustrated in Fig. 1a. Firstly, due to the presence of hydrophilic groups, GO forms a favourable dispersion in DI water. The molybdenum, tin, and sulphur precursors, $Na_2MoO_4{\cdot}2H_2O$, $SnCl_4{\cdot}5H_2O$, and thiourea, were mixed with GO solution. After stirring sufficiently, these precursors were attracted to the interface of GO by non-covalent hydrogen bonding or π–π interactions with functional groups.[5,43] Through hydrothermal treatment, the vertical MoS_2 nanosheets were anchored on the graphene sheets, accompanied with the hydrolysis of $SnCl_4{\cdot}5H_2O$ into colloidal H_2SnO_3. Then, the structural compatibility of the layered MoS_2 encapsulated with SnO_2 particles and graphene provided a strong tendency for them to form the 3D aerogel structure. In particular, the integrated aerogel structure provides a sizable surface area and active sites for energy storage.[44,45] Subsequently, an advanced facile route to coat a uniform carbon film outside the aerogel was achieved through a vapor phase polymerization and carbonization process, which produces the integrated carbon-sealed heterostructure of C@MoS_2–SnO_2@Gr. Different to the formation of some conventional carbon composites *via* hydrothermal or chemical vapor deposition, the complete ultrathin carbon film and inner graphene form a bicontinuous conductive framework, which results in both lower diffusion resistance of the ions/electrons and effective restraint for volume expansion.

The phase information and purity of the as-synthesized products were obtained using X-ray diffraction (XRD) analysis, as shown in Fig. 3a. The diffraction peaks located at 2θ values of 14.3°, 33.2°, 39.6°, and 59.1° can be assigned to the (002), (100), (103), and (110) crystal faces of hexagonal MoS_2 (JCPDS#37-1492), respectively. The featured peaks at 26.7°, 33.9°, 38.1°, and 65.7° are indexed to tetragonal rutile SnO_2 (JCPDS#41-1445) for the (110), (101), (211), and (301) planes. Clearly, the characteristic peaks for MoS_2 and SnO_2 are present in the XRD spectra of their hybrids, demonstrating the successful formation of the MoS_2–SnO_2 heterostructure. Moreover, the weak intensity of the (002) peak of MoS_2 indicated the presence of a fewer-layered structure, meanwhile the undetected graphene (002) peak demonstrated that re-stacking was effectively suppressed. Raman spectroscopy was further utilized to identify the integrated hybrids in Fig. 3b. Two characteristic peaks for MoS_2 can be observed at around 375 and 402 cm^{-1}, which correspond to the E_{2g} and A_{1g} vibration modes, respectively.[46] Compared with that for the bulk MoS_2 (30 cm^{-1}), the frequency difference (27 cm^{-1}) between the two vibration modes tends to reduce, which further demonstrates the reduced thickness of MoS_2.[43] For SnO_2@Gr, the featured

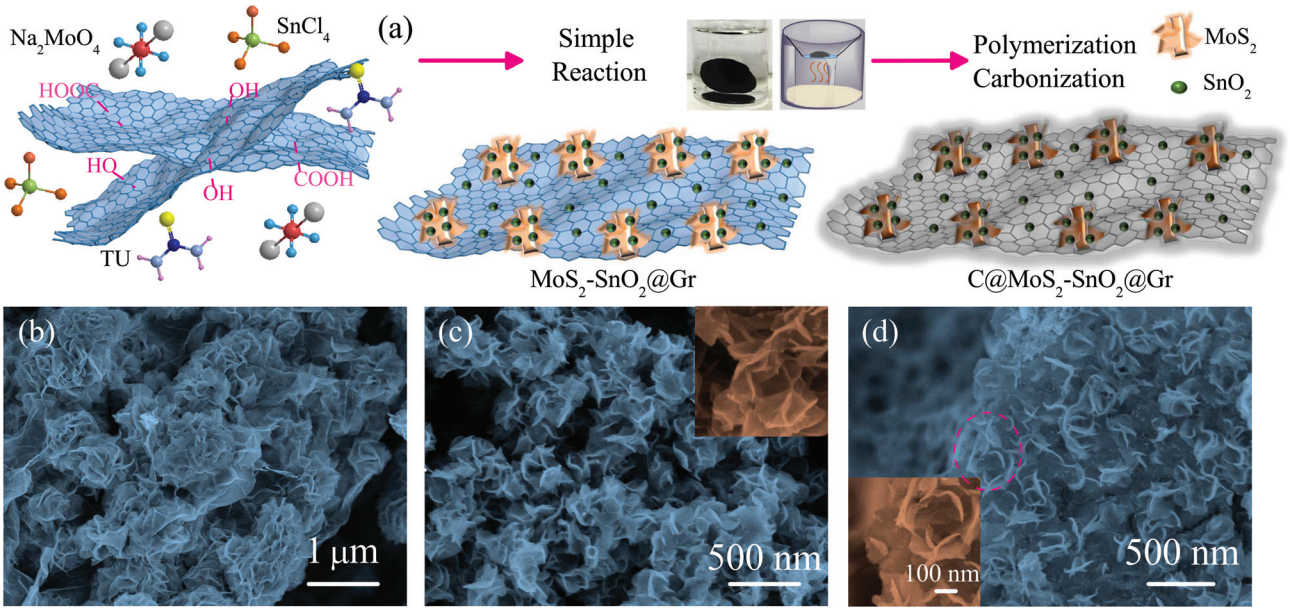

Fig. 1 (a) Schematic illustration of the fabrication procedure of the integrated C@MoS_2–SnO_2@Gr composite, including hydrothermal, vapor polymerization, and carbonization treatment. SEM images of (b) MoS_2@Gr, (c) MoS_2–SnO_2, and (d) MoS_2–SnO_2@Gr. The insets of (c) and (d) show the high magnification images.

peaks at around 474, 623, and 763 cm^{-1} can be attributed to the E_g, A_{1g}, and B_{2g} vibration modes, which relate to symmetric and asymmetric Sn–O stretching. Two distinct peaks centered at 1336 and 1586 cm^{-1} were ascribed to the D (disordered) and G (ordered) bands of graphene, shedding light on the increased number of defect sites from the reduction process.[47] Besides, for the composites, the peak intensity for SnO_2 becomes low, demonstrating the decoration of SnO_2 nanoparticles on MoS_2 and the coverage of carbon.

The evolution of the morphology and the microstructure of all the samples have been investigated using the SEM images shown in Fig. 1b–d. Without any of the SnO_2 composition, pure MoS_2 and MoS_2@Gr both tend to form bigger 3D flower microspheres aggregated by MoS_2 nanosheets with a micrometer order (Fig. 1b and Fig. S1†) due to the high surface energy, while with the participation of SnO_2, the size of the MoS_2 particles distinctly decreased to around 100–200 nanometers, which reveals that the SnO_2 nanoparticles produced a strong effect on the interlayer van der Waals attraction of MoS_2. As shown in Fig. 1d, with graphene sheets as the skeleton, SnO_2-decorated MoS_2 nanosheets evolve into multitudinous curved interlaced petals vertically anchored evenly on both sides of the whole graphene network. It is believed that the 2D SnO_2–MoS_2 units distributed on graphene could effectively enhance the interfacial contact for Li^+ and promote the ion diffusion and electrochemical activities. In particular, after coating with the carbon layer, the C@MoS_2–SnO_2@Gr composite (Fig. 2) presents a similar morphology to that of MoS_2–SnO_2@Gr, besides the obvious porous and separated puckered matrix. This could be due to the released gas and the constriction of the 3D aerogel during the vapor polymerization and carbonization procedures. Thus, one can expect that the corrugated framework provides more extra space for accommodating the volume variations and more active sites for reactions.[48–50] To verify this, the nitrogen isotherms of the as-prepared composites were recorded (Fig. S2†). Obviously, C@MoS_2–SnO_2@Gr possesses a mesoporous structure with a narrow size distribution (about 4.3 nm), as well as a much bigger specific surface area of 98.2 $m^2\ g^{-1}$ than MoS_2–SnO_2 (55.8 $m^2\ g^{-1}$) and MoS_2@Gr (44.9 $m^2\ g^{-1}$). It deserves to be mentioned that based on the resultant samples, thiourea was considered as a suitable S source using some verification experiments. Firstly, colloidal H_2SnO_3 was deduced as the cause of the $SnCl_4$ hydrolysis effect in the hydrothermal process, and then controlled experiments were conducted with different S sources (excess thioacetamide and thiourea) and the H_2SnO_3 precursor.[51] The XRD results of the collected products (Fig. S3†) show that whole SnS (JCPDS#39-0354) was obtained from thioacetamide due to the faster hydrolysis/dissociation reactions of TAA with elevated temperature.[52] With thiourea and H_2SnO_3 as the precursor, a high proportion of SnO_2 was obtained due to less reduction with a lower concentration of liberated H_2S. In addition, the XRD pattern of MoS_2–SnO_2 fabricated from H_2SnO_3, $Na_2MoO_4{\cdot}2H_2O$, and thiourea under identical conditions further corroborated the effective formation of bespoke heterostructure materials due to the formation of thiourea-based complexes and the different solubility product of MoS_2 and SnO_2.[53,54]

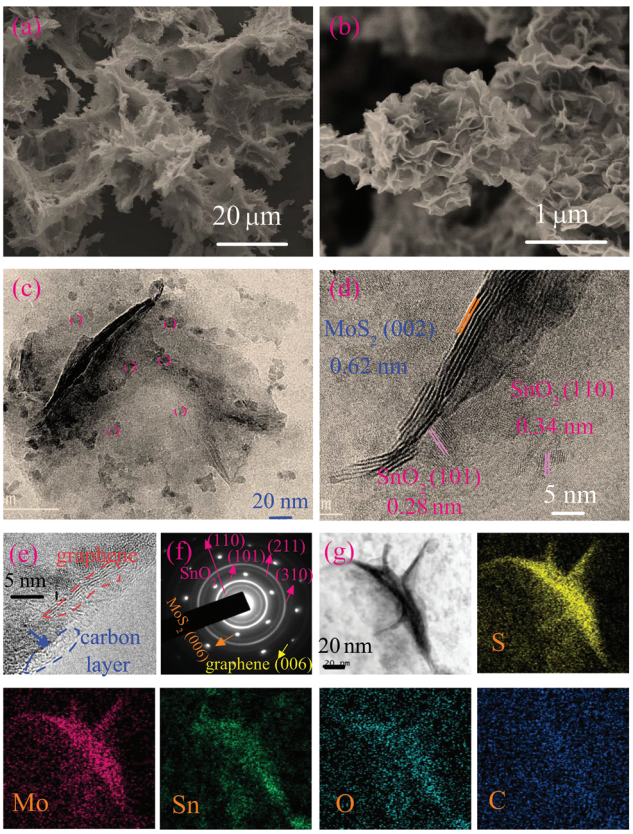

Fig. 2 (a)–(b) SEM images of C@MoS_2–SnO_2@Gr architectures at different magnifications. (c)–(d) TEM and HRTEM images of C@MoS_2–SnO_2@Gr. (e)–(g) HRTEM image of the edge of the carbon layer, the SAED pattern, and the corresponding elemental mapping images of S, Mo, Sn, O, and C, respectively.

Moreover, TEM and HRTEM characterization has been employed to reveal more specific information on the heterostructure. The cross-sectional image of the C@MoS_2–SnO_2@Gr composite in Fig. 2c confirms the unique architecture of the vertical MoS_2 petal-shaped nanosheets on the graphene matrix. Many tiny SnO_2 nanoparticles decorate the MoS_2 petals with a diameter of 5–8 nm (Fig. S4†). The HRTEM image (Fig. 2d) shows parallel lattice fringes with d = 2.8 Å and d = 3.4 Å, corresponding to the (101) and (110) planes of the SnO_2 crystal, respectively.[31,41] The MoS_2 sheets with 5–8 layers prove the lattice spacing of 6.2 Å, matching well with the (002) planes of hexagonal MoS_2.[24,27] It can be seen that the MoS_2 and SnO_2 particles are in tight contact in the hetero-interface, which improved the interfacial activity and electron transport kinetics. To corroborate this, the related cleaved crystal structure in the mechanism investigation section shows that the distance between five adjacent Sn atoms on the (101) crystal surface of SnO_2 (2.28 nm) matches well with seven intervals of S–S on the (001) crystal surface of MoS_2 (0.32 nm × 7), accounting for the generation of covalent force and available growth of the heterostructure. The selected area electron diffraction

(SAED) pattern (Fig. 2f), taken from part of Fig. 2c, further proves the mixed phase nature of the integrated C@MoS_2–SnO_2@Gr composite. Specifically, the bright diffraction spots and diffraction rings can be indexed to the reflections of the MoS_2 (002) and (006) planes, the graphene (201) plane, and the SnO_2 (110), (101), (211), and (310) planes, which are marked in Fig. 2f. In order to accurately confirm the elemental composition and spatial distribution, elemental mapping analysis was performed (Fig. 2g). The well-proportioned distributions of C, S, Mo, Sn, and O can be obtained from the mapping results. Moreover, the wrinkled fringes in Fig. 2e indicate the graphene conductive matrix and the feature of the ultrathin carbon layer at the edge (about 2 nm), which can accelerate the diffusion of electrons/ions. To further certify the presence of the carbon layer, TGA and EDS were conducted (Fig. 3f and Fig. S5†). The weight loss in MoS_2–SnO_2@Gr is attributed to the formation of MoO_3 from MoS_2 and the oxidation of GO. According to the 2 : 1 element ratio of Mo to Sn (Fig. S5†), the amount of graphene in MoS_2–SnO_2@Gr is about 6%. Thus, the amounts of carbon and graphene in C@MoS_2–SnO_2@Gr are about 1% and 6%, respectively. Taking the loss of GO in the annealing process and the extra carbon adsorption in the EDS measurement into consideration, the above results agree well with those of the EDS analysis (11%) and the theoretical value (over 8%). It is believed that the ultrathin carbon layer could bring whole coverage and restraint of the inner hetero-hybrids to ensure high structural stability during the cycling process.

The information on the chemical composition and valence states of the C@MoS_2–SnO_2@Gr composites was obtained using X-ray photoelectron spectroscopy (XPS). Fig. S6† displays the XPS survey spectra of the as-fabricated products. The result for C@MoS_2–SnO_2@Gr reveals the main presence of O, C, S, Mo, and Sn elements, containing all the distinctive peaks of both MoS_2@Gr and SnO_2@Gr. As displayed in Fig. 3c, the C 1s spectrum can be categorized into three main peaks, centered at 284.8, 286.2, and 288.7 eV for sp^2 C=C, C–N, and C=O, respectively. Note that the absence of C–O reflects the reduction of GO into graphene during the carbonization process. According to the high resolution Mo 3d analysis in Fig. 3d of C@MoS_2–SnO_2@Gr, two dominant peaks at 230.21 eV and 233.36 eV could be assigned to Mo $3d_{5/2}$ and Mo $3d_{3/2}$, respectively.[55] A shoulder peak at 227.18 eV has also been fitted, corresponding to S 2s. In Fig. 3e, the binding energy peaks at 488.28 eV and 496.78 eV are due to Sn $3d_{5/2}$ and Sn $3d_{3/2}$.[40] Notably, in the integrated 3D architecture of C@MoS_2–SnO_2@Gr, the Mo 3d and Sn 3d peaks shift toward a lower binding energy (shaded lines) compared with those of the

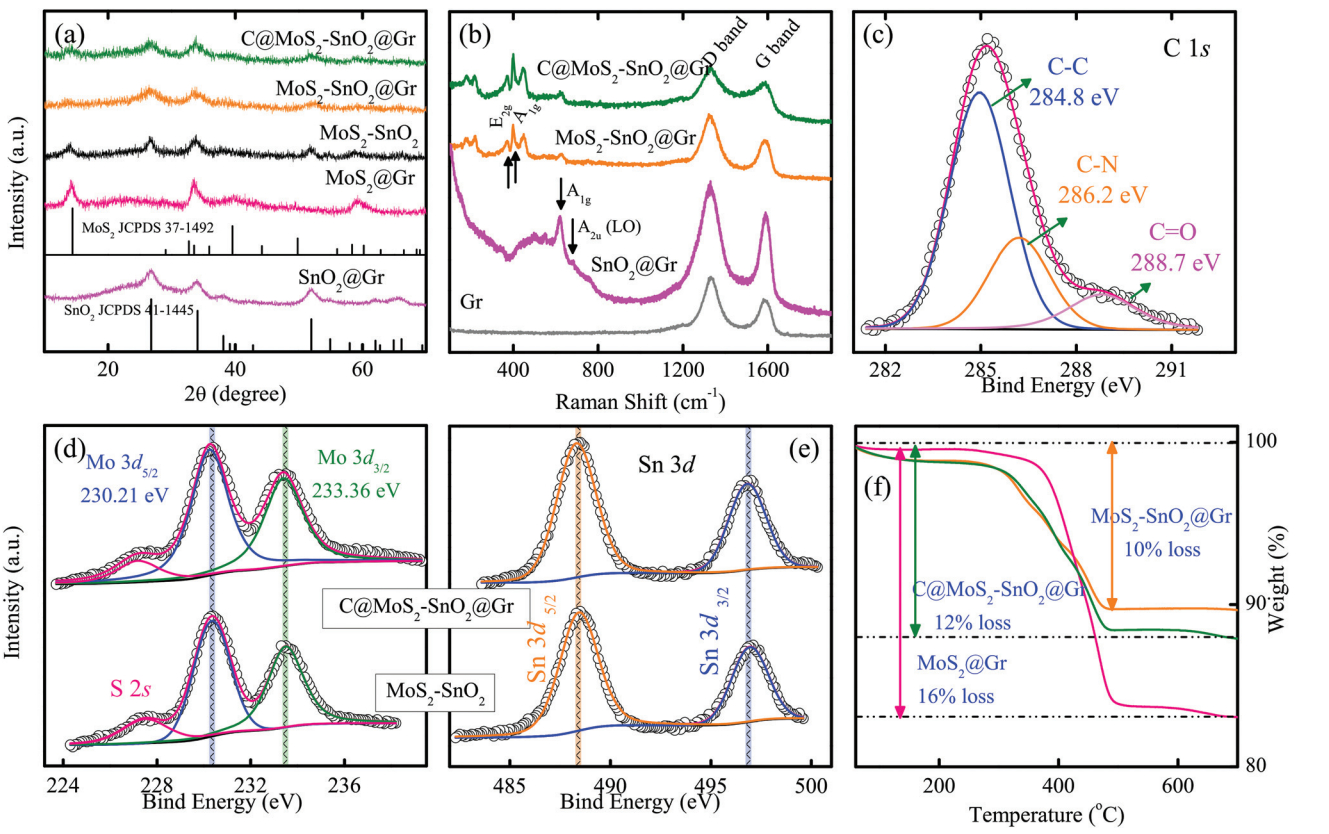

Fig. 3 (a) XRD patterns and (b) Raman spectra of the as-prepared composites. (c) The high resolution C 1s spectrum of C@MoS_2–SnO_2@Gr. The high resolution (d) Mo 3d and (e) Sn 3d spectra of the C@MoS_2–SnO_2@Gr and MoS_2–SnO_2@Gr composites. Note that the scatter plots and solid lines indicate the experimental data and fitted results, respectively. The shaded lines indicate the peak shifts of Mo 3d and Sn 3d.

MoS_2–SnO_2 hybrids, MoS_2@Gr, and SnO_2@Gr. The related results of MoS_2@Gr and SnO_2@Gr have also been fitted (Fig. S6†). This might be due to the coverage of the C film and related electronic shielding synergistic effect of the heterostructure.[34,56] Taking the spin–orbit separation into consideration, the phenomena of the Mo 3d (3.15 eV) and Sn (8.5 eV) peaks disclose the existence of Mo^{4+} and Sn^{4+} based on the reported results.

In Fig. 4a, the cyclic voltammetry (CV) curves of the electrode for the integrated C@MoS_2–SnO_2@Gr were recorded to investigate the Li ion storage mechanism. In the first cathodic process, a broad peak appears at 1.02 V, which is assigned to the intercalation of Li ions into the MoS_2 layers to form Li_xMoS_2 (eqn (α): $MoS_2 + xLi^+ + xe^- \leftrightarrow Li_xMoS_2$).[31,49] The shoulder peak near to 0.85–0.75 V could be attributed to the reduction process (eqn (β): $SnO_2 + 4Li^+ + 4e^- \rightarrow Sn + 2Li_2O$) and the formation of the solid electrolyte interphase (SEI) layer, which is an irreversible process. The next peak at around 0.4 V corresponds to the conversion reaction (eqn (γ): $MoS_2 + 4Li^+ + 4e^- \leftrightarrow Mo + 2Li_2S$). In addition, extra cathodic peaks located at 0.1–0.05 V represent the reversible formation of Li_xSn alloys (eqn (λ): $Sn + xLi^+ + xe^- \leftrightarrow Li_xSn$) and the lithium insertion in carbon ($C + xLi^+ \leftrightarrow Li_xC$), respectively. It can be seen that shift phenomena occurred in the CV curves of the MoS_2@Gr and SnO_2@Gr hybrids (Fig. S7†), further elucidating the synergistic effects on the electrochemical properties of the heterostructure. In the following oxidation scan, two main oxidation peaks at 0.6 and 1.32 V are ascribed to the reversible de-alloying reaction of Sn and Li and the partial conversion of Sn to SnO_2.[50] Actually, the poor reversibility can be improved by the enhanced conductivity of the composites and better electric contact among fine Li_xSn and Li_2O. It can be proven that in the CV curves for SnO_2@Gr (Fig. S7†), the corresponding reduction peaks at 1.3 eV show a blue shift and gradually fade away due to the inferior reaction kinetics and serious aggregation of SnO_2. Another peak emerges at 2.25 V, which suggests the delithiation process of Li_2S. Notably, the second cathodic cycle includes a broad region at 1.82 V, which is associated with the conversion from S_8 to polysulfides, and this cannot be found in the CV curves for SnO_2@Gr.[57] Meanwhile, the subsequent CV profiles were highly overlapped, implying the reversible behavior of electrochemical performance and leading to the excellent cycling stability of the C@MoS_2–SnO_2@Gr anode materials.

The galvanostatic discharge–charge (GDC) curves (1st, 2nd, 10th, 50th, and 100th cycles) of the as-prepared electrodes at 0.1 A g^{-1} between 0.02 and 3 V are shown in Fig. 4b and Fig. S8.† The first discharge profile of the C@MoS_2–SnO_2@Gr anode consists of a flat plateau near 1.1 V and a wide slope plateau in the range of 0.8–0.55 V. Consistent with the CV results, they were produced by the intercalation of Li^+ and the conversion reaction. The initial discharge and charge capacities of the C@MoS_2–SnO_2@Gr composites are as high as 1520 and 1230 mA h g^{-1}, with a higher coulombic efficiency of around 80% compared with that of MoS_2–SnO_2@Gr, MoS_2@Gr, or SnO_2@Gr. The corresponding initial capacity

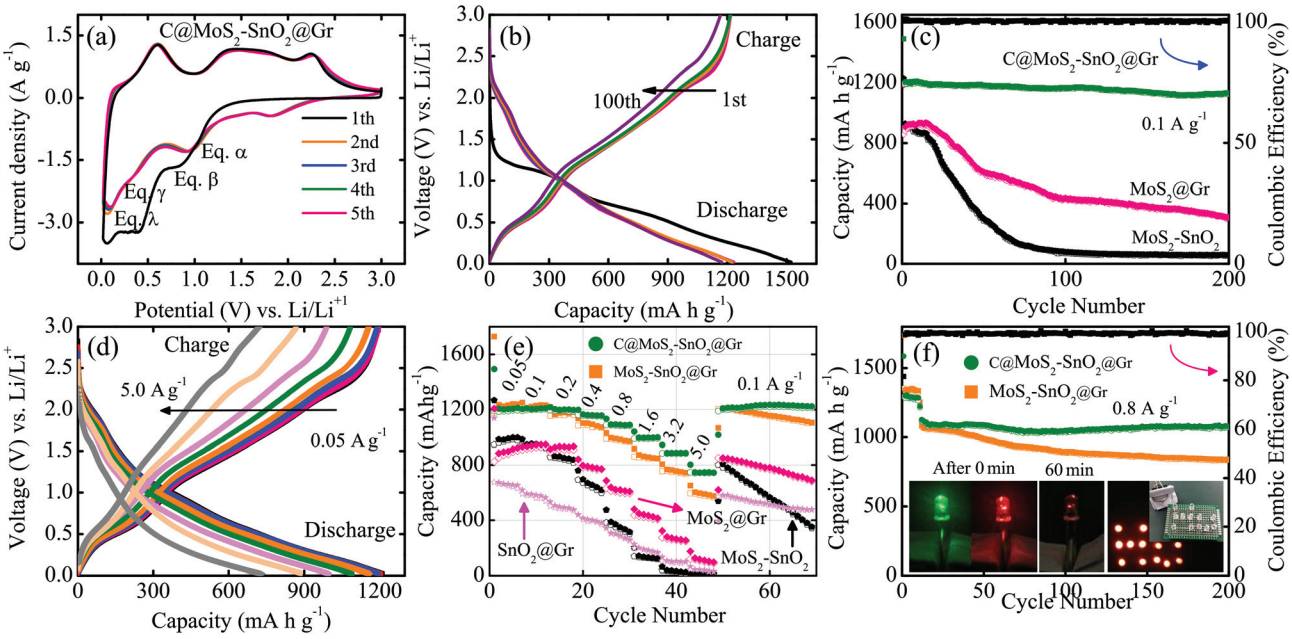

Fig. 4 Electrochemical performance of the C@MoS_2–SnO_2@Gr anode electrode. (a) CV curves for the first five cycles. (b) The GDC profiles of C@MoS_2–SnO_2@Gr for the 1st, 2nd, 10th, 50th, and 100th cycles at 0.1 A g^{-1}. (c) Cycling performance of the as-synthesized composites at 0.1 A g^{-1} for 200 cycles. Note that the mass loading of the C@MoS_2–SnO_2@Gr electrode is 2.5 mg cm^{-2}. (d) The GDC profiles of C@MoS_2–SnO_2@Gr at increasing discharge current density from 0.05 to 5.0 A g^{-1}. (e) Rate performance of the as-assembled batteries. (f) Cycling stability of C@MoS_2–SnO_2@Gr and MoS_2–SnO_2@Gr at 0.8 A g^{-1}. The inset shows the lit LEDs at 0 min and 60 min and the symbol of our Hu group on a circuit board, respectively.

loss can be ascribed to the partial conversion of SnO_2 and irreversible formation of the SEI layer on the electrode surface. Notably, the experimental capacities of the anodes are higher than the theoretical capacities of SnO_2 or MoS_2. Actually, the alloying reaction was assumed to be irreversible with the theoretical capacity of SnO_2, while the related process was largely ameliorated in the present work based on the analysis of the CV and GDC curves.[26,58] As a result, the high oxidization of Sn to SnO_2 enables it to deliver a considerable capacity. In addition, the ultrathin carbon film could enhance the electron collection pathway, together with the inner graphene matrix. Besides, the reaction benefits from the dominant pseudocapacitance contribution (above 90%), which further improves the charge transfer kinetics, and this will be discussed in detail. Significantly, almost consistent GDC curves were obtained from the second cycle and an outstanding capacity of 1170 mA h g^{-1} was achieved even after 300 cycles (Fig. S9†). The appreciable capacity retention of 95% (relative to the second discharge) indicates that the carbon layer plays a critical role in protecting the inner matrix from mechanical stress and ensuring the electrochemical stability. Although it has a high reversible capacity and relative stability, the performance of MoS_2–SnO_2@Gr gradually faded (1250 to 1000 mA h g^{-1}) due to the repeated damage of the inner structure during the lithium ion insertion/extraction processes. In particular, without the novel vertical construction of the heterostructure or protection of the carbon layer, dramatic capacity decays of the MoS_2@Gr and MoS_2–SnO_2 electrodes are evident (Fig. 4c) (with lower retentions below 35%). For comparison, as elucidated in Fig. 4c, a higher mass loading of the C@MoS_2–SnO_2@Gr anode (about 2.5 mg cm^{-2}) was evaluated. As expected, slight capacity degradation cannot be avoided, which is related to the increased internal resistance and overpotential.[59]

The rate performance of the active materials was evaluated at high current densities from 0.05 A g^{-1} to 5.0 A g^{-1}, as displayed in Fig. 4e, with the corresponding discharge–charge curves in Fig. 4d. The C@MoS_2–SnO_2@Gr composites display a prominent rate property with capacities of 1200 to 900 mA h g^{-1} when gradually elevating the current density from 0.05 A g^{-1} to 5.0 A g^{-1}. In contrast, other controlled anode materials show poor rate behaviors, especially serious capacity decreases at each rate stage, produced by the lack of contact between the electrodes and current collectors and the lack of a buffer layer to release stress. Notably, when reducing the current density back to 0.1 A g^{-1}, a reversible capacity around 1200 mA h g^{-1} was even achieved and this remained stable for 20 cycles. This can be attributed to the gradual penetration of electrolyte *via* the carbon layer and subsequently the activation of the anode materials.[60] Besides, with a high-rate GDC test at 0.8 A g^{-1}, C@MoS_2–SnO_2@Gr also presents a superior capacity of 1080 mA h g^{-1} after 200 cycles (Fig. 4f), far beyond the diminishing capacities obtained with MoS_2–SnO_2@Gr. This strongly shows that the coverage of the carbon layer can not only restrain the agglomeration of MoS_2 nanosheets and SnO_2 nanoparticles, but also shorten the distance for electron transport. These are believed to be essential to guarantee the remarkable capacity stability in some recent works on MoS_2 or SnO_2 graphene-based anode materials (Table S1†).[23,41,49,61–63] Also, a red/green colored light-emitting diode (LED) indicator has been powered by the assembled LIB (Fig. 4f). The red lights still remained bright after 60 min, while the green one became weaker after 10 min due to its demand for a high voltage. Interestingly, a symbol of our Hu group has been powered on a circuit board. To inspect the durability of the C@MoS_2–SnO_2@Gr electrode, a high rate assessment for 2000 cycles at 2.5 A g^{-1} was performed (Fig. 5a). Interestingly, it goes through quick fading, stabilization, increasing, and durability stages. Evidently the electrode suffered from the formation of the SEI layer and due to the partial irreversibility of the reaction of Sn to SnO_2 particles, it degrades quickly and maintains a lower capacity for about 800 cycles after the initial capacity of 1000 mA h g^{-1}. Meanwhile, along with the deeper activation and the remission of the pin effect of small particles on the graphene matrix and SEI film, an increase in the lithium ion storage was observed. Finally, the C@MoS_2–SnO_2@Gr electrode delivers a capacity of around 680 mA h g^{-1} after 2000 cycles and realizes excellent durability and reversibility. However, MoS_2@Gr shows serious degradation, which corroborates the advantages of the unique architecture and the synergistic effects between SnO_2 and vertical MoS_2 sheets.

To further verify the durability and high rate behavior, the conceivable surface capacitance characteristics were investigated for the energy storage kinetics of the C@MoS_2–SnO_2@Gr anodes. As shown in Fig. 6a, the CV curves at scan rates from 0.1 to 5 mV s^{-1} show the basic characteristics. Along with the gradual lithiation, the dominant mechanism between the surface capacitive and diffusion-controlled mechanisms can be distinguished from the relation: $i = av^b$,[38,39] where i and v are the current and sweep rate, respectively, and a and b are appropriate values. For the semi-infinite linear diffusion-limited process, the current is proportionate to $v^{1/2}$, while for the capacitive process, it relates to v. Thus, two cathodic and anodic peak b values (Fig. 6b) are fitted to be about 0.96 and 0.9, respectively. The higher b value than those of MoS_2@Gr (0.71) and SnO_2@Gr (0.73) indicates the capacitive-dominated kinetics and faster charge transfer of the C@MoS_2–SnO_2@Gr electrode (Fig. S10†). According to the general relationship $i = k_1v^{1/2} + k_2v$, the contribution of surface capacitance effects can be obtained by calculating the fraction of k_1 and k_2 at each potential.[64] Quantitatively, a capacitive contribution of higher than 91% was confirmed from the inner region in Fig. 6c at 1 mV s^{-1}, which is much higher than that for MoS_2@Gr (Fig. 6e). Besides, this proportion becomes more dominant with the increase of scan rate, which can be found in the statistic histogram of the two electrodes (Fig. S11†). In detail, for the C@MoS_2–SnO_2@Gr electrode, the relative capacitive contributions varied from 89% to 96% from 0.1 to 5 mV s^{-1}, higher than those for several reported oxide and sulfide electrodes.[36] As a result, all of these quantified results match well with the b values above and shed light on the enhanced reaction kinetics in the vertical 3D architecture. To further validate the

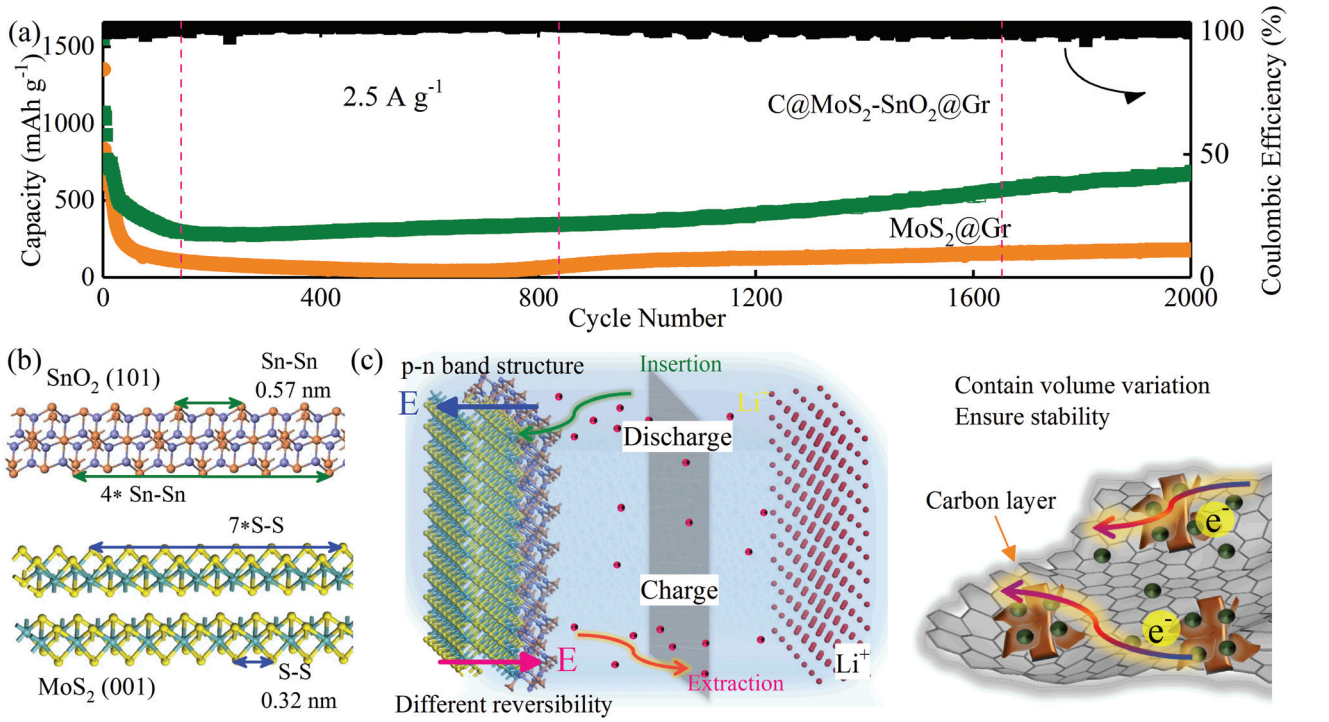

Fig. 5 (a) Durable rate cycling of C@MoS_2–SnO_2@Gr and MoS_2@Gr at 2.5 A g^{-1} for 2000 cycles. (b) The cleaved crystal structure of MoS_2 and SnO_2 with the (001) and (101) crystal planes, respectively. (c) The half-cell structure and the improved transfer kinetics mechanism of C@MoS_2–SnO_2@Gr for LIB applications.

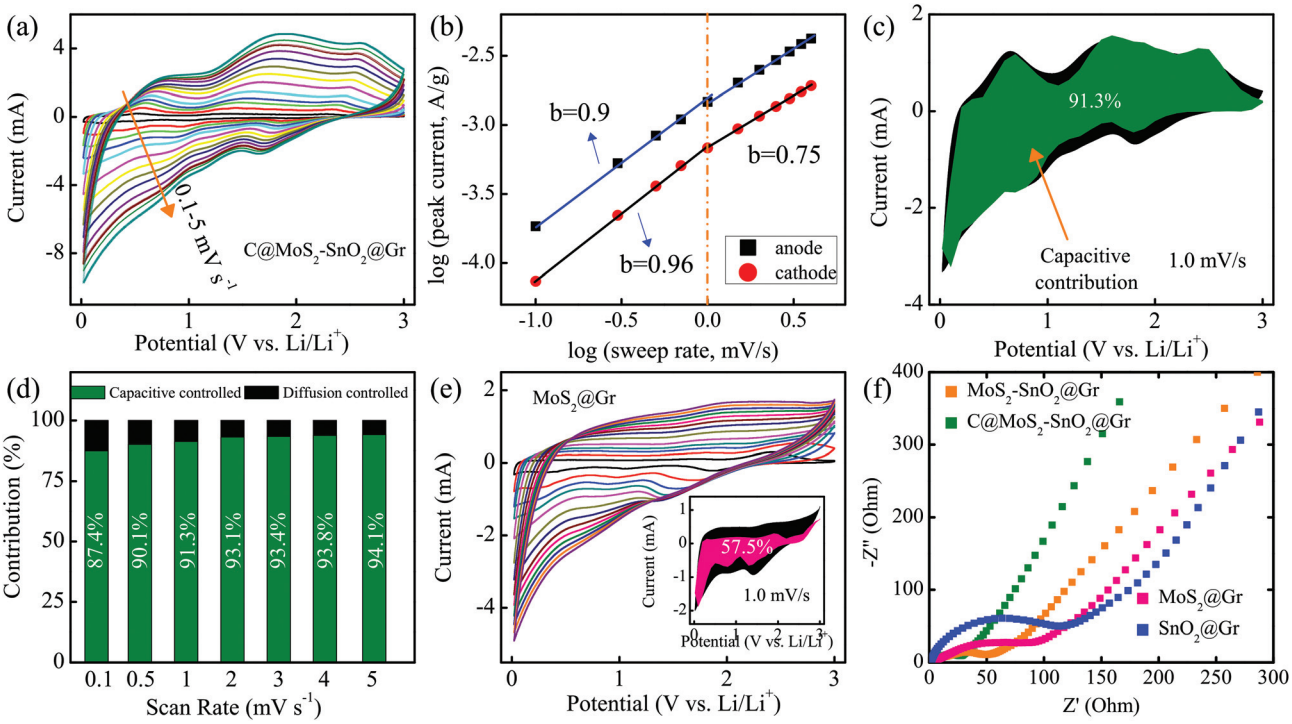

Fig. 6 The pseudocapacitance mechanism analysis of C@MoS_2–SnO_2@Gr electrodes. (a) CV curves at various rates from 0.1–5 mV s^{-1}. (b) The fitted specific anodic/cathodic peak current for determining the *b* value. (c) Capacitive (green) and diffusion-controlled (black) contributions of C@MoS_2–SnO_2@Gr at 1 mV s^{-1}. (d) Normalized contribution ratio of capacitive contribution at various rates. (e) CV curves at various rates from 0.1–5 mV s^{-1} for the MoS_2@Gr electrode. The inset is the related capacitive contribution at 1 mV s^{-1}. (f) The electrochemical impedance spectra of the as-prepared samples.

advantages of the composites, electrochemical impedance spectra of all of the anode materials were collected. In Fig. 6f, the smaller diameter of the semicircle at the high–medium frequency region and the greater slope at the lower frequency region for the C@MoS_2–SnO_2@Gr electrode indicate the lowest charge transfer resistance.[15] It is believed that the results are highly coincident with the better electrochemical performance and improved charge transfer kinetics for the novel C@MoS_2–SnO_2@Gr electrode.

Consequently, combined with the above pseudocapacitance effect and the synergistic effect of the heterostructure, a reasonable mechanism was proposed in terms of the superior behavior in Li^+ storage applications. Generally, p-type MoS_2 can be easily obtained by an aerogel process based on previous studies, and SnO_2 works as an n-type semiconductor.[31,47,65] The band edge positions can be calculated according to the empirical formula: $E_{VB} = X - E^e + 0.5E_g$. Note that E_{VB} is the valence band (VB) edge potential and E^e refers to the free electron energy on the hydrogen scale (4.5 eV), and X is the electronegativity of the corresponding semiconductor, expressed as the geometric mean of the electronegativity for the component atoms. Based on previous studies, the E_{VB} and E_{CB} (CB, the conduction band) of MoS_2 are approximately estimated to be 0.1 eV and 1.4 eV, with ΔE_{VB} = 2.15 eV and ΔE_{CB} = 0.18 eV, respectively, compared to those of SnO_2, which are used to estimate the relative band edge positions of MoS_2 and SnO_2.[56,66] Thus, based on the investigation of the crystal surface matching of the hybrid (Fig. 5b), a built-in electric field from SnO_2 nanoparticles to MoS_2 nanosheets could be introduced by the diffusion of carriers at the MoS_2–SnO_2 p–n hetero-interface. In the discharge process, the induced electric field would promote Li^+ transfer and insertion from the surface SnO_2 nanoparticles to the inner MoS_2 nanosheets. Meanwhile, in the charge process, due to the facile reversible reaction of MoS_2 and SnO_2, a potential difference and a reversed electric field at the interface would be generated from MoS_2 and SnO_2 (Fig. 5c). Therefore, this could form a reversed driving force to facilitate the electron/ion diffusion among fine nanoparticles and the extraction of Li^+ from Li_2O. In addition, the 3D graphene aerogel and ultrathin carbon layer endow the electrode with improved conductivity and avoid the localization and aggregation of Li_xSn, which enables favourable reversible conversion. As strong evidence, the structural evolution of the C@MoS_2–SnO_2@Gr electrode after the GDC process at 2.5 A g^{-1} is provided. In Fig. 7, the layered MoS_2 anchored on the graphene matrix can be identified, with numerous fine SnO_2 particles dispersed on it. In particular, compared with the particles before GDC cycles and the survey of SnO_2 after the GDC cycles, the SnO_2 nanoparticles in the C@MoS_2–SnO_2@Gr electrode are still well distributed (Fig. 7d and Fig. S12†). Therefore, the restrained aggregation phenomenon during the lithiation and delithiation process emphasized the ameliorative reversibility, which sequentially endows the C@MoS_2–SnO_2@Gr electrode with a higher initial coulombic efficiency and durable rate performance.

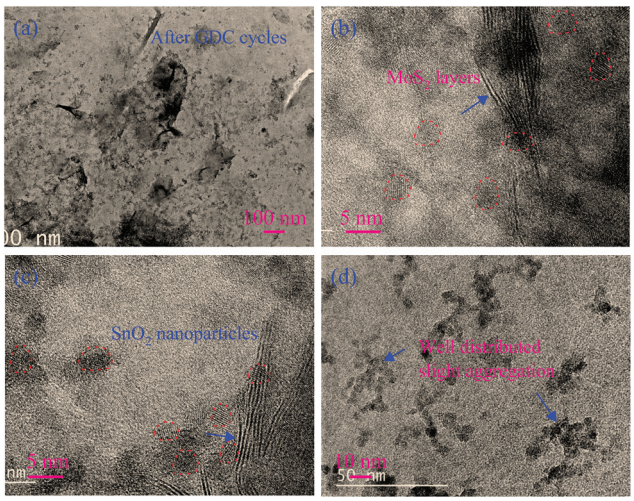

Fig. 7 (a) TEM images and (b)–(c) HRTEM analysis of the C@MoS_2–SnO_2@Gr electrode after GDC cycles at 2.5 A g^{-1}. The parallel-layered MoS_2 and featured lattice fringes of SnO_2 have been marked. (d) The well-distributed SnO_2 nanoparticles on graphene after the cycles reveals the slight aggregation of the electrode.

4. Conclusions

In summary, a simple and effective method, the vapor polymerization/carbonization method, was developed to coat an ultrathin carbon layer on a MoS_2–SnO_2–graphene anode for boosting LIB performance. The novel heterostructure exhibits a reversible capacity with a high ICE up to 80% (0.1 A g^{-1} current density) and delivers a stable capacity of 680 mA h g^{-1} at 2.5 A g^{-1} with a long lifetime (2000 cycles). Accordingly, these enhanced performances should be attributed to the following. (I) The uniform encapsulation of the carbon layer with the 3D graphene aerogel matrix forms a bicontinuous conductive network to facilitate electron/ion diffusion. (II) Based on the analysis of the band structure and crystal surface matching of the composites, the internal driving force and better electric contact can effectively improve the reversibility and retain the aggregation of fine particles. (III) Quantitative analysis of the surface capacitive contribution reasonably explains the enhanced kinetics and durable high rate performance. Therefore, the integrity of the structure and dominant pseudocapacitance effect in the kinetics of transition metal-based electrodes both established a promising paradigm for energy storage systems.

Conflicts of interest

There are no conflicts to declare.

Acknowledgements

One of the authors (M. J. Li) would like to thank Dr C. Li for constructive discussions. This work was financially supported

by the Major State Basic Research Development Program of China (Grant No. 2013CB922300), the Natural Science Foundation of China (Grant No. 61674057, 11374097, 61376129, 61504156, and 61227902), the Projects of Science and Technology Commission of Shanghai Municipality (Grant No. 15JC1401600 and 14XD1401500), and the Program for Professor of Special Appointment (Eastern Scholar) at Shanghai Institutions of Higher Learning.

References

1 F. Y. Cheng, J. Liang, Z. L. Tao and J. Chen, *Adv. Mater.*, 2011, **23**, 1695–1715.
2 S. H. Choi, Y. N. Ko, J.-K. Lee and Y. C. Kang, *Adv. Funct. Mater.*, 2015, **25**, 1780–1788.
3 J.-M. Tarascon and M. Armand, *Nature*, 2011, **414**, 359–367.
4 P. G. Bruce, B. Scrosati and J.-M. Tarascon, *Angew. Chem., Int. Ed.*, 2008, **47**, 2930–2946.
5 X. Q. Xie, Z. M. Ao, D. W. Su, J. Q. Zhang and G. X. Wang, *Adv. Funct. Mater.*, 2015, **25**, 1393–1403.
6 C. B. Zhu, X. K. Mu, P. A. van Aken, J. Maier and Y. Yu, *Adv. Energy Mater.*, 2015, **5**, 1401170.
7 M. H. Modarres, J. H.-W. Lim, C. George and M. D. Volder, *J. Phys. Chem. C*, 2017, **121**, 13018.
8 H. P. Cong, S. Xin and S. H. Yu, *Nano Energy*, 2015, **43**, 7295.
9 H. J. Tang, J. Y. Wang, H. J. Yin, H. J. Zhao, D. Wang and Z. Y. Tang, *Adv. Mater.*, 2015, **27**, 1117–1123.
10 X. Li, C. F. Zhang, S. Xin, Z. C. Yang, Y. T. Li, D. W. Zhang and P. Yao, *ACS Appl. Mater. Interfaces*, 2016, **8**, 21373–21380.
11 J. P. Yang, Y. X. Wang, S. L. Chou, R. Y. Zhang, Y. F. Xu, J. W. Fan, W. X. Zhang, H. K. Liu, D. Y. Zhao and S. X. Dou, *Nano Energy*, 2015, **18**, 133–142.
12 Z. Tang, C. H. Tang and H. Gong, *Adv. Funct. Mater.*, 2012, **22**, 1272–1278.
13 K. Wang, H. P. Wu, Y. N. Meng and Z. X. Wei, *Small*, 2014, **10**, 14–31.
14 P. Y. Tang, L. J. Han, A. Genç, Y. M. He, X. Zhang, L. Zhang, J. R. Galán-Mascarós, J. R. Morante and J. Arbiol, *Nano Energy*, 2016, **22**, 189–201.
15 X. H. Xia, D. L. Chao, C. F. Ng, J. Y. Lin, Z. X. Fan, H. Zhang, Z. X. Shen and H. J. Fan, *Mater. Horiz.*, 2015, **2**, 237–244.
16 J. Zhu, Z. Xu and B. G. Lu, *Nano Energy*, 2014, **7**, 114–123.
17 Y. X. Tang, J. Y. Deng, W. L. Li, O. I. Malyi, Y. Y. Zhang, X. R. Zhou, S. W. Pan, J. Q. Wei, Y. R. Cai, Z. Chen and X. D. Chen, *Adv. Mater.*, 2017, **29**, 1701828.
18 Y. X. Tang, Y. Y. Zhang, X. H. Rui, D. P. Qi, Y. F. Luo, W. R. Leow, S. Chen, J. Guo, J. Q. Wei, W. L. Li, J. Y. Deng, Y. K. Lai, B. Ma and X. D. Chen, *Adv. Mater.*, 2016, **28**, 1567.
19 Y. X. Tang, Y. Y. Zhang, J. Y. Deng, D. P. Qi, W. R. Leow, J. Q. Wei, S. Yin, Z. L. Dong, R. Yazami, Z. Chen and X. D. Chen, *Angew. Chem., Int. Ed.*, 2014, **53**, 13488.
20 Y. X. Tang, Y. Y. Zhang, W. L. Li, B. Ma and X. D. Chen, *Chem. Soc. Rev.*, 2015, **44**, 5926.
21 Y. X. Tang, Y. Y. Zhang, J. Y. Deng, J. Q. Wei, H. L. Tam, B. K. Chandran, Z. L. Dong, Z. Chen and X. D. Chen, *Adv. Mater.*, 2014, **26**, 6111.
22 Y. J. Gong, S. B. Yang, L. Zhan, L. L. Ma, R. Vajtai and P. M. Ajayan, *Adv. Funct. Mater.*, 2014, **24**, 125–130.
23 F. Y. Xiong, Z. Y. Cai, L. B. Qu, P. F. Zhang, Z. F. Yuan, O. K. Asare, W. W. Xu, C. Lin and L. Q. Mai, *ACS Appl. Mater. Interfaces*, 2015, **7**, 12625–12630.
24 Y. Wang, B. Chen, D. H. Seo, Z. J. Han, J. I. Wong, K. Ostrikov, H. Zhang and H. Y. Yang, *NPG Asia Mater.*, 2016, **8**, e268.
25 Y. Zhang, Y. Q. Yu, L. F. Mi, H. Wang, Z. F. Zhu, Q. Y. Wu, Y. G. Zhang and Y. Jiang, *Small*, 2016, **8**, 1062–1071.
26 S. Karmakar, C. Chowdhury and A. Datta, *J. Mater. Chem. A*, 2016, **120**, 14522–14530.
27 C. J. Hsu, C. Y. Chou, C. H. Yang, T. C. Lee and J. K. Chang, *Chem. Commun.*, 2016, **52**, 1701–1704.
28 J. Zhu, K. Sakaushi, G. Clavel, M. Shalom, M. Antonietti and T. P. Fellinger, *J. Am. Chem. Soc.*, 2015, **137**, 5480–5485.
29 X. Zhao, J. H. Sui, H. T. Fang, H. E. Wang, J. Y. Li, W. Cai and G. Z. Cao, *Nanoscale*, 2016, **8**, 17902.
30 F. K. Meng, J. T. Li, S. K. Cushing, M. J. Zhi and N. Q. Wu, *J. Am. Chem. Soc.*, 2013, **135**, 10286–10289.
31 B. Huang, X. Li, Y. Pei, S. Li, X. Cao, R. C. Massé and G. Z. Cao, *Small*, 2016, **12**, 1945–1955.
32 L. L. Wang, Z. Lou, R. Zhang, T. T. Zhou, J. N. Deng and T. Zhang, *ACS Appl. Mater. Interfaces*, 2016, **8**, 6539–6545.
33 D. Z. Zhang, Y. E. Sun, P. Li and Y. Zhang, *ACS Appl. Mater. Interfaces*, 2016, **8**, 14142–14149.
34 Y. Zheng, T. F. Zhou, C. F. Zhang, J. F. Mao, H. K. Liu and Z. P. Guo, *Angew. Chem., Int. Ed.*, 2016, **55**, 3408–3413.
35 M. H. Wang, H. Yang, X. L. Zhou, W. Shi, Z. Zhou and P. Cheng, *Chem. Commun.*, 2016, **52**, 717–720.
36 Y. Jiang, Y. B. Guo, W. J. Lu, Z. Y. Feng, B. J. Xi, S. S. Kai, J. H. Zhang, J. K. Feng and S. L. Xiong, *ACS Appl. Mater. Interfaces*, 2017, **9**, 27697–27706.
37 V. Augustyn, J. Come, M. A. Lowe, J. W. Kim, P.-L. Taberna, S. H. Tolbert, H. D. Abruña, P. Simon and B. Dunn, *Nat. Mater.*, 2013, **12**, 518–522.
38 D. L. Chao, C. R. Zhu, P. H. Yang, X. H. Xia, J. L. Liu, J. Wang, X. F. Fan, S. V. Savilov, J. Y. Lin, H. J. Fan and Z. X. Shen, *Nat. Commun.*, 2016, **7**, 12122.
39 S. Li, J. X. Qiu, C. Lai, M. Ling, H. J. Zhao and S. Q. Zhang, *Nano Energy*, 2015, **12**, 224–230.
40 L. Xia, S. Q. Wang, G. X. Liu, L. X. Ding, D. D. Li, H. H. Wang and S. Z. Qiao, *Small*, 2016, **12**, 853–859.
41 X. F. Du, T. J. Yang, J. Lin, T. Y. Feng, J. B. Zhu, L. Lu, Y. L. Xu and J. P. Wang, *ACS Appl. Mater. Interfaces*, 2016, **8**, 15598.
42 W. S. Hummers and R. E. Offerman, *J. Am. Chem. Soc.*, 1958, **80**, 1339.
43 Y. G. Li, H. L. Wang, L. M. Xie, Y. Y. Liang, G. S. Hong and H. J. Dai, *J. Am. Chem. Soc.*, 2011, **133**, 7296.

44 L. Chen, B. Wei, X. T. Zhang and C. Li, *Small*, 2013, **9**, 2331–2340.
45 R. Sun, H. Y. Chen, Q. W. Li, Q. J. Song and X. T. Zhang, *Nanoscale*, 2014, **6**, 12912.
46 H. Li, Q. Zhang, C. C. Ray Yap, B. K. Tay, T. H. Tong Edwin, A. Olivier and D. Baillargeat, *Adv. Funct. Mater.*, 2012, **22**, 1385.
47 F. Carraro, L. Calvillo, M. Cattelan, M. Favaro, M. Righetto, S. Nappini, I. Píš, V. Celorrio, D. J. Fermín, A. Martucci, S. Agnoli and G. Granozzi, *ACS Appl. Mater. Interfaces*, 2015, **7**, 25685.
48 Y. Liu, X. Z. Wang, X. D. Song, Y. F. Dong, L. Yang, L. X. Wang, D. Z. Jia, Z. B. Zhao and J. S. Qiu, *Carbon*, 2016, **109**, 461–471.
49 L. F. Jiang, B. H. Lin, X. M. Li, X. F. Song, H. Xia, L. Li and H. B. Zeng, *ACS Appl. Mater. Interfaces*, 2016, **8**, 2680.
50 J. Q. Shan, Y. X. Liu, P. Liu, Y. S. Huang, Y. Z. Su, D. Q. Wu and X. L. Feng, *J. Mater. Chem. A*, 2015, **3**, 24148–24154.
51 J. Zeng, M. D. Xin, K. W. Li, H. Wang, H. Yan and W. J. Zhang, *J. Phys. Chem. C*, 2008, **112**, 4159.
52 R. Thangappan, S. Kalaiselvam, A. Elayaperumal, R. Jayavel, M. Arivanandhan, R. Karthikeyan and Y. Hayakawa, *Dalton Trans.*, 2016, **45**, 2637.
53 G. Z. Shen, D. Chen, K. B. Tang, F. Q. Li and Y. L. Qian, *Chem. Phys. Lett.*, 2003, **370**, 334.
54 Y. J. Chen, G. H. Tian, Q. X. Guo, R. Li, T. R. Han and H. G. Fu, *CrystEngComm*, 2015, **17**, 8720.
55 S. G. Wang, X. Li, Y. Chen, X. J. Cai, H. L. Yao, W. Gao, Y. Y. Zheng, X. An, J. L. Shi and H. R. Chen, *Adv. Mater.*, 2015, **27**, 2775.
56 M. J. Li, J. Y. Wang, P. Zhang, Q. L. Deng, J. Z. Zhang, K. Jiang, Z. G. Hu and J. H. Chu, *Sci. Rep.*, 2017, **7**, 42484.
57 X. H. Cao, B. Zheng, X. H. Rui, W. H. Shi, Q. Y. Yan and H. Zhang, *Angew. Chem., Int. Ed.*, 2016, **53**, 1404–1409.
58 Y. Tang, D. Wu, S. Chen, F. Zhang, J. Jia and X. Feng, *Energy Environ. Sci.*, 2013, **6**, 2447–2451.
59 H. T. Sun, L. Mei, J. F. Liang, Z. P. Zhao, C. Lee, H. L. Fei, M. N. Ding, J. Lau, M. F. Li, C. Wang, X. Xu, G. L. Hao, B. Papandrea, I. Shakir, B. Dunn, Y. Huang and X. F. Duan, *Science*, 2017, **356**, 599–604.
60 Y. Z. Su, Y. X. Liu, P. Liu, D. Q. Wu, X. D. Zhuang, F. Zhang and X. L. Feng, *Angew. Chem., Int. Ed.*, 2015, **54**, 1812–1816.
61 Y. G. Huang, Q. C. Pan, H. Q. Wang, C. Ji, X. M. Wu, Z. Q. He and Q. Y. Li, *J. Mater. Chem. A*, 2016, **4**, 7185.
62 T. N. Y. Khawula, K. Raju, P. J. Franklyn, I. Sigalas and K. I. Ozoemena, *J. Mater. Chem. A*, 2016, **4**, 6411–6425.
63 F. Ye, B. T. Zhao, R. Ran and Z. P. Shao, *J. Power Sources*, 2015, **290**, 61–70.
64 D. Chao, P. Liang, Z. Chen, L. Bai, H. Shen, X. Liu, X. Xia, Y. Zhao, S. V. Savilov, J. Lin and Z. X. Shen, *ACS Nano*, 2016, **10**, 10211–10219.
65 R. Marschall, *Adv. Funct. Mater.*, 2013, **24**, 2421–2440.
66 Y. C. Zhang, Z. N. Du, K. W. Li, M. Zhang and D. D. Dionysiou, *ACS Appl. Mater. Interfaces*, 2011, **3**, 1528.